



FRONTIERS ARTICLE

Enhancing image contrast and slicing electron pulses in 4D near field electron microscopy

Sang Tae Park, Ahmed H. Zewail*

Physical Biology Center for Ultrafast Science and Technology, Arthur Amos Noyes Laboratory of Chemical Physics, California Institute of Technology, Pasadena, CA 91125, USA

ARTICLE INFO

Article history:

Available online 22 November 2011

ABSTRACT

In this Letter, we discuss the use of photon-induced near field electron microscopy (PINEM) to reach new limits of temporal and spatial resolutions. We invoke two optical femtosecond pulses, one of them is for the usual clocking of dynamical change but the second one is for gating (slicing) the imaging-electron continuous or pulsed beam. It is shown that in both cases the resolution becomes that of the optical gating pulse and not of the electron one. We also show that by using the near field of a nanoparticle it is possible to enhance contrast in imaging of materials and including biological structures.

© 2011 Elsevier B.V. All rights reserved.

1. Introduction

In recent years, 4D ultrafast electron microscopy (UEM) and diffraction (UED) have been developed for the study of structural dynamics of isolated molecules, surfaces, and nanostructures [1]. Because single-electron imaging is introduced, it is possible to reach the atomic-scale resolutions, spatially and temporally [2]. In principle, the temporal resolution is determined by three main contributions; the excitation laser pulse duration, the electron packet duration, and the velocity mismatch between them [3]. In practice, high voltage fluctuation and electronic jitter may also contribute. Optical pulses with duration below 10 fs are now commercially available, and a generation of attosecond extreme ultraviolet (XUV) pulses [4] has been demonstrated [5–7]. Group velocity mismatch can be overcome in reflection electron diffraction geometry, using a tilted optical pulse arrangement [8], and when the transmission geometry of UEM is utilized, it is not of concern; for a specimen thickness of up to 100 nm, the mismatch in time is 1 fs (femtosecond). Accordingly, further improvement of the time resolution requires control of the electron pulse duration.

Electron packets in ultrafast diffraction and microscopy are generated by femtosecond photoemission and acceleration to the kinetic energy of 30–200 keV, typically with an extraction electric fields of $\sim 10^6$ V/m. An initial emission energy spread of more than 0.1 eV results from the laser-pulse energy width and the distribution of energies determined by the work function of the cathode material [9]. This energy distribution is directly related to the width of the electron packet [10]: $\Delta t \approx \frac{d\Delta E}{v_i E_f}$, where ΔE is the energy spread and v_i and E_f are the initial velocity and final energy, respectively; d is the distance of the cathode from the anode. For exam-

ple, for $\Delta E = 0.1$ eV, and typical d of 0.5 mm and E_f corresponding to 1 kV, the pulse width is 300 fs, and for larger ΔE , the width further increases [11]. Several schemes have been proposed for the generation or compression of ultrashort electron pulses [12–20].

Here, the behavior of electron packets in the near field of a nanostructure is exploited for slicing the pulses and enhancing image contrast. The strong interaction of free electrons and photons, mediated by a nanostructure (such as carbon nanotube, silver nanowire, protein vesicle, or *Escherichia coli* cell) is the key for the success of photon-induced near field electron microscopy (PINEM) [21,22]. The theoretical basis of the phenomenon was developed in Ref. [23] to account for various observations made. In this Letter, we discuss the new findings which support the concept of gating in PINEM, which makes the temporal resolution limited only by the optical pulse profile, and the near field spatial localization which leads to the enhancement of contrast in imaging.

2. PINEM field and imaging

Free electrons generally do not interact with light in vacuum as the coupling is not permitted due to momentum-energy mismatch. The mismatch condition can be overcome in certain circumstances such as inverse Cerenkov radiation [24], inverse Smith–Purcell radiation [25], Kapitza–Dirac effect [26], laser-assisted electron/atom scattering [27,28], among others. As described elsewhere [23], these effects have their origin in different interaction terms of the Hamiltonian ($\vec{A} \cdot \vec{p}$ or A^2 , where \vec{A} is the vector potential and \vec{p} the momentum); for the latter effect [27,28] the electron scatters from the potential of the atom modified by the photon interaction. In these various schemes, neither the ultrafast temporal resolution was introduced nor the spatial imaging can reach that of UEM. Moreover in PINEM, the nanostructure is central to mediating the electron-photon interaction.

* Corresponding author. Address: 1200 E. California Blvd., m/c 127-72, Caltech, Pasadena, CA 91125, USA. Fax: +1 626 796 8315.

E-mail address: zewail@caltech.edu (A.H. Zewail).

When light is scattered by a nanostructure, the near field component exhibits a momentum spread, due to its spatial confinement ($\Delta x \Delta p \approx \hbar$). Furthermore, the scattering gives rise to a longitudinal component of the electric field resulting in acceleration/deceleration of the electron packet. This component at the spatial frequency that corresponds to the electron momentum change makes possible the coupling and the exchange of many quanta of photon energy. The PINEM field is given by (see Eq. (A.12) and text above in Ref. [23]):

$$\tilde{F}\left(\frac{\omega_p}{v_e}\right) = \int_{-\infty}^{+\infty} dz'' \tilde{E}_z(z'', 0) \exp\left[-i\left(\frac{\omega_p}{v_e}\right)z''\right], \quad (1)$$

which is the Fourier transform component of the longitudinal electric field of scattered light wave at the spatial frequency of $\Delta k_e = k_e^f - k_e^i = \frac{\Delta p_e}{\hbar} = \frac{\omega_p}{v_e}$. In Eq. (1), $\tilde{E}(\vec{r}, t)$ is the complex representation of the electric field of scattered light, ω_p is the angular frequency of photon, and v_e is the electron velocity. The near field is relatively huge when compared with far-field detections; it is determined by the spatial geometry of the nanostructure and strength of the electric field of the incident wave, and its dielectric response in the material. It follows that due to this field the imaging electron will display in the energy domain quantized gain/loss peaks with different orders (n) i.e., $\pm n\hbar\omega_p$. It can be shown that the n th order intensity is directly related to $|\tilde{F}|^{2n}$, in the weak interaction limit (see Section 4.3.1 in Ref. [23]). In the strong interaction limit, the intensity is expressed in terms of a Bessel function. We note that the integration is over z which is the direction of the electron propagation, and an image in the x - y direction, obtained in parallel beam illumination, maps the field distribution of the object. Conversely, an electron beam convergent at a given (x, y) point gives the field at this particular point in space.

Because the interaction is via a particular component of scattered light, the degree of interaction depends on the distance of electron trajectory from the scattering center (electron impact parameter, b), and the incident polarization angle with respect to electron propagation trajectory. The polarization changes according to a cosine function. The PINEM field decreases exponentially as the impact parameter increases, with the decay length being on the nanoscale. With PINEM imaging, we can map the spatial profile of the field by selecting only electrons that have gained photon energy and recording the energy-selected, dark field, image. The contrast is strongest at the projected nanoscale interface and when the field is captured prior to its decay on the fs time scale. Light scattering and energy exchange are instantaneous, and, therefore, the temporal profile of the entire response is determined by the convolution of the two beams, the optical pulse and electron packet.

3. Three pulse gating

In order to illustrate the effect of gating electron packets using optical pulses and the role of the near field, we use the solution of the time-dependent Schrödinger equation for a free electron under the influence of a scattered electromagnetic wave [23]. The final, post-scattering wavefunction is given as a summation over discrete momentum/energy states:

$$\Psi(z + \infty) = g(z - v_e t, -\infty) \sum_{n=-\infty}^{\infty} \left(-\tilde{F} / |\tilde{F}| \right)^n J_n(\Omega) \exp[i(k_n z - \omega_n t)], \quad (2)$$

where $J_n(\Omega)$ is the Bessel function of the first kind [29], whose argument is given by $\Omega(z'; \tau) = \frac{e}{\hbar\omega_p} |\tilde{F}| \exp\left[-\frac{(z' - v_e \tau)^2}{4v_e^2 \sigma_p^2}\right]$. Here, $z' = z - v_e t$, and σ_p and τ are the photon pulse duration and time delay between electron and photon pulses, respectively. The frequencies and

momenta are simply given by: $\omega_n = \omega_e + n\omega_p$ and $k_n = k_e + n(\omega_p/v_e)$, which express the energy and momentum of the electron after a net n photon absorption/emission. Finally, the envelope function of the initial state, which is taken to be of a Gaussian profile, can be written as: $g(z - v_e t, -\infty) = \left(\frac{1}{\sqrt{2\pi}v_e\sigma_e}\right) \exp\left[-\frac{(z - v_e t)^2}{2v_e^2\sigma_e^2}\right]$.

It is more convenient to transform $P(z)$, $\Psi\Psi^*$, the propagating wavepacket intensity spatial distribution at given time, into $P(t')$, flux or the temporal profile at a fixed position. Using $P(z)dz = P(t')dt'$, where the arrival time, $t' \approx -z'/v_e = -(z - v_e t)/v_e$, is defined with respect to the center of the packet, we obtain the n th state (sub-packet) intensity as:

$$P_n(t') = P_e(t')Q_n(t'; \tau), \quad (3)$$

where $P_e(t') = v_e |g(-v_e t', -\infty)|^2 = \frac{1}{\sqrt{2\pi}\sigma_e} \exp\left[-\frac{t'^2}{2\sigma_e^2}\right]$ is the electron total intensity (temporal) profile and $Q_n(t'; \tau) = |J_n(\Omega(t'; \tau))|^2$ is the n th order transition probability density. The properties of Bessel function, $J_n(\Omega) \rightarrow 0$ as $\Omega \rightarrow 0$ for $n \neq 0$, dictates that the PINEM intensity becomes significant only during the optical pulse duration, i.e. when $|t'| < \sigma_p \ll \sigma_e$ at $\tau = 0$. Therefore, the pulse duration of the electron packet that has gained energy becomes comparable to that of the photon pulse duration, and it even becomes shorter than the optical duration for higher n . This is the basis of the slicing concept; one optical pulse is used for the gating of the electron packet and another for the clocking of the event.

The temporal gating scheme is illustrated in Figure 1. An electron packet (blue) is generated in UEM and arrives at the nanostructure (yellow circle) where it overlaps with the optical gate pulse (green). The 'sub-packet' of the electron which temporally coincides with the optical gate pulse will either gain or lose kinetic energy that equals to multiples of photon energy. Since the electron-photon energy exchange occurs only when the electron, photon, and the particle are at the same time and in the same place, we can use this concept of PINEM to ultrafast-gate the electron packet with a very narrow temporal and spatial window. This gating results in the slicing of the electron packet and in that sense can be likened to slicing, using wigglers, of femtosecond X-rays from synchrotron radiation [30,31]. However, our approach utilizes the nanostructure for slicing and the electron packet is not required to be relativistic as in the case of synchrotron radiation.

The above described approach can be used to switch a continuous electron beam or to slice a pulse. Figure 2a shows the case of continuous beam gated by a fs pulse, following a fs pump pulse, and with a system decay time of 500 fs. In Figure 2b, the individual sub-packets of the electron which gained multiple photon

Electron Pulse Slicing, PINEM

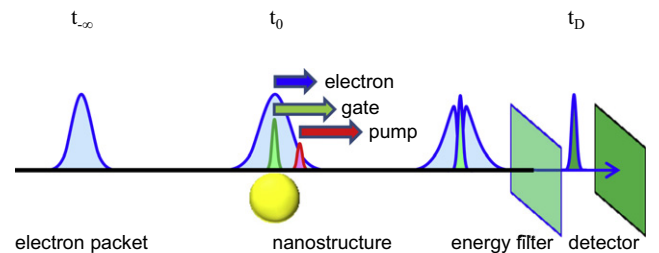


Figure 1. Schematic of experimental slicing mechanism. The initial electron packet (blue) overlaps with the optical gate pulse (green) at the nanostructure (yellow circle). The optical pump pulse (red) initiates the dynamics with a time delay from the gate pulse. The arrows depict relative propagation velocities. The zeroth order ($n = 0$) state is depleted as a result of photon-electron energy exchange but with a duration comparable to that of the gate pulse. The cut-off energy filter is for selection of PINEM intensities for electrons which gained energy from the photons (see text).

Electron-Beam Switching

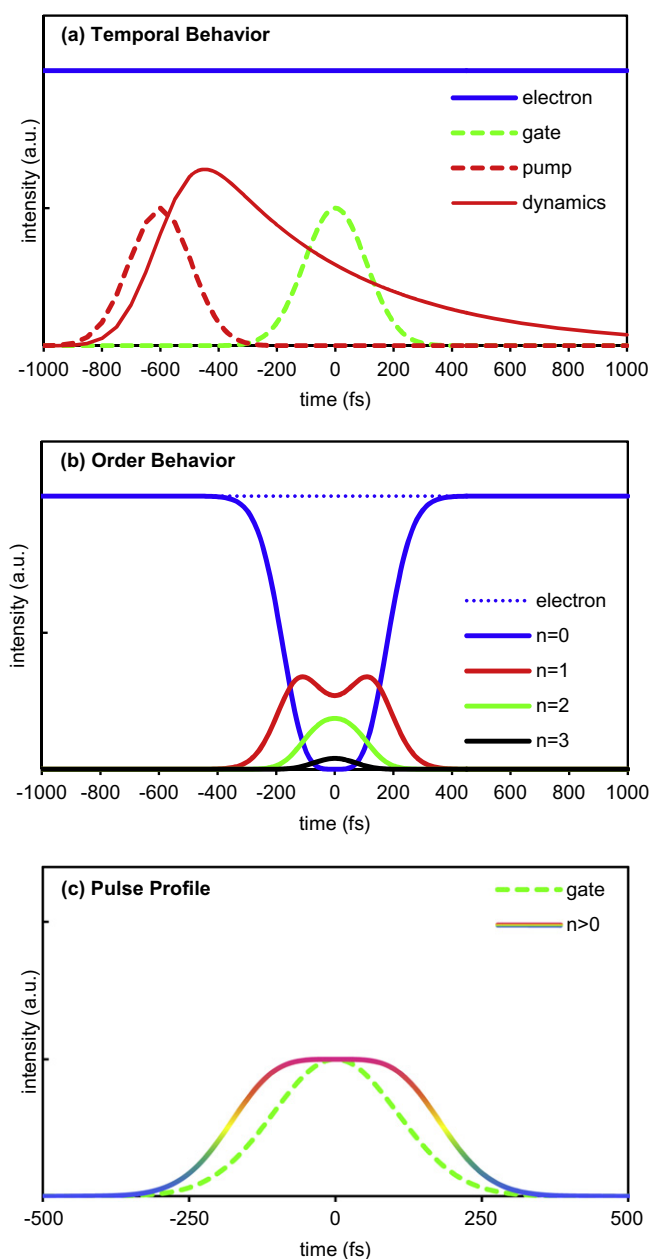


Figure 2. Electron continuous-beam switching. (a) Temporal behavior of the gate and pump optical pulses ($\sigma_p = 106$ fs), and the continuous electron beam ($\sigma_e \rightarrow \infty$). (b) Order behavior of the temporal profiles of the populations of electrons for different orders ($n = 0, 1, 2, 3, \dots$). (c) Comparison of the gated electron packet (rainbow) and the gate optical pulse profile (dotted green). The saturation feature is due to the large depletion of $n = 0$ peak.

energies, and the zeroth order sub-packet (blue) which is depleted by the optical gate pulse, are displayed. The full width half maximum (FWHM) of the optical pulse is 250 fs ($\sigma_p = 106$ fs). For this case, where the electron beam is continuous ($\sigma_e \rightarrow \infty$) i.e., not pulsed, the gate actually creates a pulsed beam. By adjusting the delay time between the gate pulse (green) and the optical pump pulse (red), the dynamics clocked by the pump pulse can be investigated with an ultrafast temporal resolution when selecting those electrons with a higher kinetic energy. It is to be noted that higher n energy exchanges have a narrower width, of course with a decrease in intensity; in the weak interaction limit $\sigma'_n \approx \sigma_p / \sqrt{n}$ (see Eq. (26) in Ref. [23]). Figure 2c compares the temporal profiles of the optical

Electron-Pulse Slicing

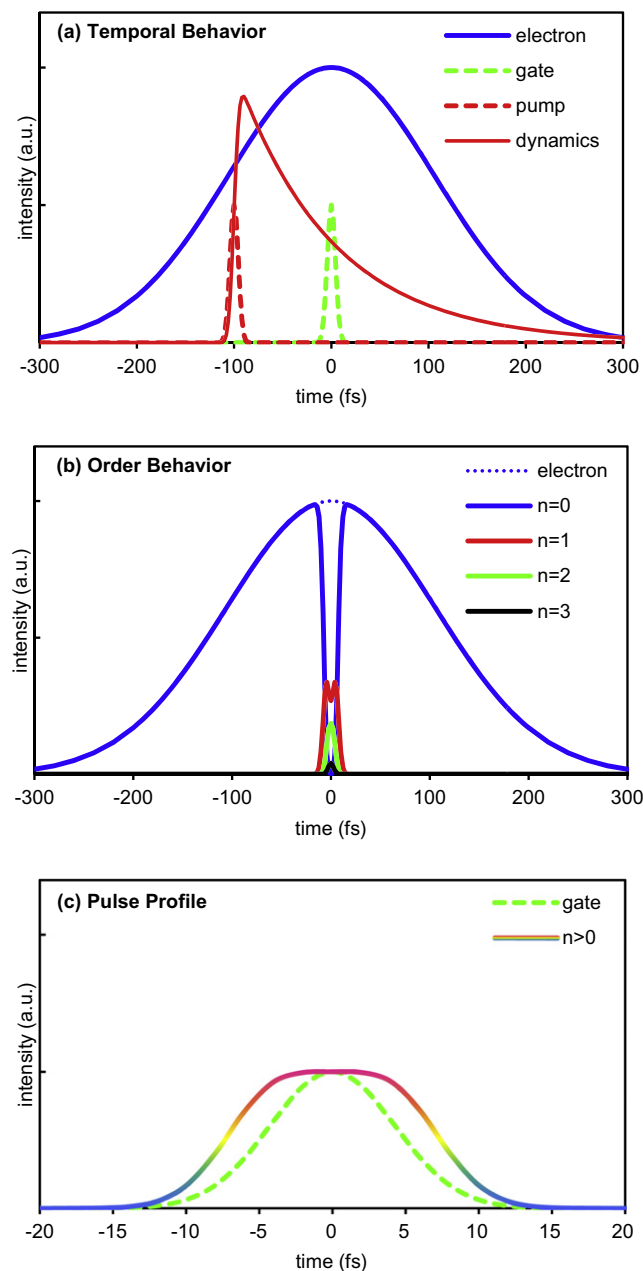


Figure 3. Electron pulse slicing. (a) Temporal behavior of the gate and pump optical pulses ($\sigma_p = 4$ fs), and the pulsed electron beam ($\sigma_e = 106$ fs). (b) Order behavior of temporal profiles of the populations of electrons for each order ($n = 0, 1, 2, 3, \dots$). (c) Comparison of the gated electron packet (rainbow) and the gate optical pulse (dotted green). The saturation feature is due to the large depletion of $n = 0$ peak.

gate pulse and the electron sub-packet (rainbow) with higher kinetic energies, i.e., $P_+(t'; n > 0) = \sum_{n=1}^{+\infty} P_n(t')$. In Figure 2c, shown is the switching of the continuous beam into a pulsed beam with duration comparable to the width of the gating pulse; the saturation is because of the large depletion at the fluence used.

Next we considered a broad electron packet and used the optical pulses and nanostructure for slicing it. In Figure 3, we show the results for $\sigma_e = 106$ fs and $\sigma_p = 4$ fs. In this case, we expect effective shortening of the electron pulse down to the optical pulse width. The results in Figure 3 confirm this hypothesis and provide a novel methodology for reaching a few femtosecond and possibly attosecond, resolution, in UEM. Figure 3a and b give the temporal and order behavior whereas Figure 3c depicts the pulse profile.

Several advantages are worth noting. First, although the temporal resolution becomes limited by the duration of the optical gate pulse, no band pass filter is needed. In other words, a high pass filter is enough in this approach; the energy-gained electrons, $n \geq 1$, are selected. In this case, when $n = 1$, $\hbar\omega_p = 2.39$ eV at 519 nm. A band pass filter whose energy width is chosen according to the temporal resolution desired can, in principle, improve the temporal resolution [32], but in PINEM higher temporal and spatial resolutions are controlled by the near field of the nanostructure. Another advantage of the approach is the elimination of jitter, because gating is done optically and fluctuation in electron energy and in electronics, which result in a temporal broadening, becomes irrelevant. A third one is that the scheme is also spatially selective as it is possible to image on the nanoscale, because the field integral, \tilde{F} , decays exponentially with distance from the nanostructure with a decay length of nearly a , the radius of nanosphere.

Even though the effect is strong enough to completely deplete the $n = 0$ peak (Figures 2 and 3), the optical gate pulse overlaps with the electron for a very short time, leaving unchanged portions of the electron packet which do not coincide with the optical gate pulse. The efficiency of conversion can be written as $1/2(\sigma_p/\sigma_e)$, where a factor of half arises from the fact that we only select the sub-packet that gained energy. Naturally, care has to be taken to make sure that the optical gate pulse does not induce unwanted dynamics and the excitation clocking pulse does not cause any photon energy exchange with the electron packet. The tunability and fluence of fs optical pulses are two parameters that can be varied for these selectivities.

4. Contrast enhancement and single particle imaging

Light scattering by nanostructures is treated using the Mie equation [33], but when the particle size is much smaller than the optical wavelength, Rayleigh dipole approximation [34] is invoked. The PINEM field, \tilde{F} , can be evaluated numerically using the Mie solution and analytically using the Rayleigh (near field) approximation. For a sphere, \tilde{F} outside the particle ($b > a$) is given by:

$$\tilde{F} = -i(\tilde{E}_0 \cos \phi) \chi_s 2a^2 \Delta k_e \{ \Delta k_e a K_1(\Delta k_e b) \}, \quad (4)$$

where E_0 , ϕ , and χ_s are, respectively, the electric field amplitude, the laser polarization angle, and the spherical susceptibility defined as $\chi_s = (\tilde{n}^2 - 1)/(\tilde{n}^2 + 2)$. The impact parameter is b , and a is again the radius of the particle. K_1 is the modified Bessel function of the second kind [29]. The curly bracket in Eq. (4) exhibits an exponentially decaying function of the impact parameter, and the $1/e$ decay length, δ , of the PINEM field in the exponential decay regime [23] is given by $-\frac{1}{\delta} = \lim_{b \rightarrow a} \frac{\partial \log \tilde{F}}{\partial b}$. For small spheres, the decay length reaches the radius value, $\delta = a$. Therefore, the PINEM field in this case is only significant within a length scale that is comparable to the particle size.

When the electron propagates through the material ($b < a$), the integration for the PINEM field, \tilde{F} , needs to be done piecewise for the regions outside and inside the material. An analytical expression for the field for such a case cannot be obtained, and it has to be numerically evaluated. Nevertheless, it is expected that the field should decrease as the electron trajectory approaches the center of the particle, due to the symmetry of the scattered wave. Figure 4 shows the PINEM field (divided by the incident electric field amplitude, E_0) for 5 nm radius gold particle at 519 nm illumination. (Unlike the case of the three pulse scheme described in the previous section, here we only employ one laser which is coincident with the electron pulse.) It indicates that the PINEM field is (almost linearly) proportional to the impact parameter for $b < a$, and exponen-

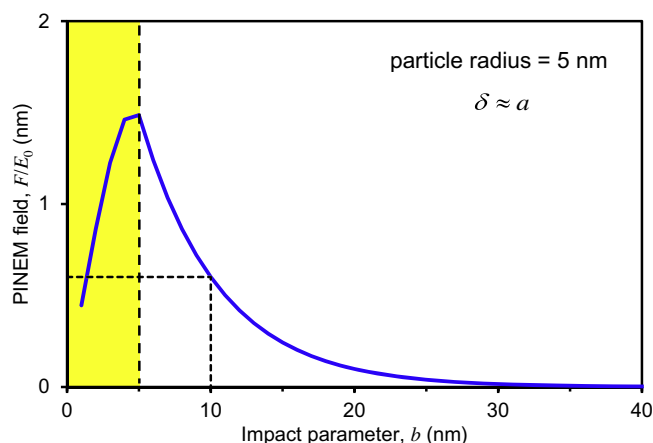


Figure 4. Spatial localization on the nanoscale. Shown is the dependence of the PINEM field on the impact parameter, b , inside and outside of a 5 nm radius nanoparticle of gold. Note the exponential behavior outside the particle interface, in this case vacuum.

tially decays for $b > a$, as indeed expected physically. The decay length scale is similar to that of the particle radius.

This feature of spatial localization here we exploit for contrast enhancement and for PINEM imaging that may be relevant to immunolabeling of cells. Figure 5 illustrates the scheme where a nanoparticle inside a cell is imaged by PINEM. A cell (either native or frozen) is placed in vacuum (or dielectric medium). A 10 nm diameter gold particle attached to an antibody specific to an antigen is placed inside the cell. The cell is then illuminated with a femtosecond laser light, of which a fraction is transmitted and is scattered by the nanoparticle inside. Depending on the geometry of the cell, the transmitted light wave inside the cell may be refracted and/or slightly converged. However, the wave can be still approximated as a planar one, with a refracted angle, for a relatively small particle.

Figure 6 depicts the results for the spatial profiles of bright-field (electron transmission) and dark-field (PINEM image) intensities using a 10 nm gold (or protein) particle in 500 nm whole or sectioned cell. The PINEM signal is generated by the particles (gold or protein) and by the cell membrane due to their evanescent scatterings, and these are the interface areas that will 'light up'. For the gold particle ($\tilde{n} = 0.64 + 2.05i$) [35], the wavelength of 519 nm is near the Fröhlich resonance [36] at 2.53 eV, which enhances absorption and scattering. In the case of the green fluorescence protein ($\tilde{n} = 1.5$), light is off resonance with the absorption at 479 nm (the stronger absorption peak is at 395 nm). Because of the spatial localization discussed above, the PINEM image exhibits a bimodal intensity profile with sharp maxima at the interfaces.

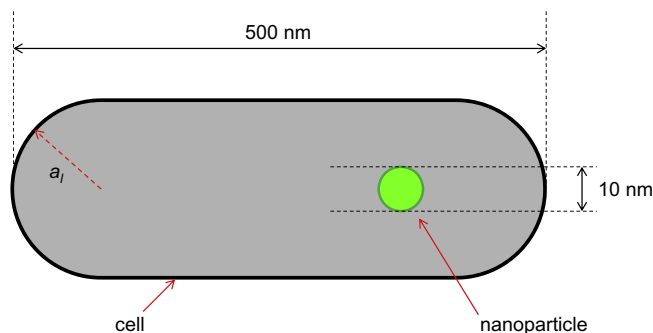


Figure 5. PINEM imaging of a single particle in a dielectric medium. Schematic of the gold nanoparticle in a cell. The dimension of the cell is not to scale.

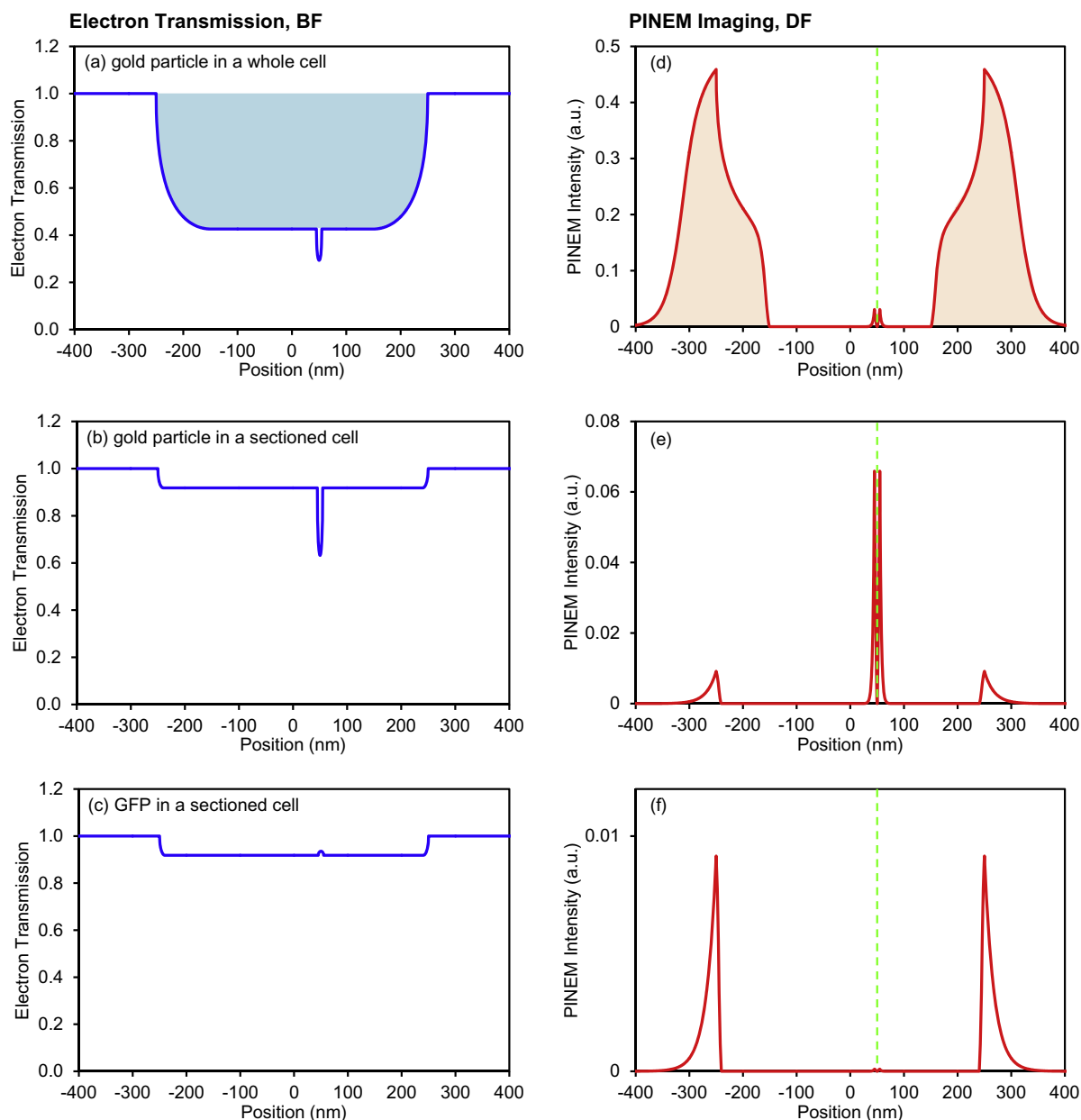


Figure 6. Electron transmission (bright field) and PINEM (dark field) imaging. Bright-field (left) and PINEM (right) images of (a) the gold particle in a whole cell, (b) the gold particle in a sectioned cell, and (c) the green fluorescent protein in a sectioned cell. Note the contrast difference and the background-free feature of PINEM, DF imaging.

Such profile enables one to precisely locate the particles (interfaces) from the PINEM images. More importantly is the enhanced PINEM contrast at the particle position (green dotted line) inside the cell.

One significant advantage of PINEM imaging is that it is background free, the analogue of dark field imaging but without conventional diffraction selection. This feature greatly enhances the contrast, as can be seen in the results of Figure 6, especially for sectioned cells when the thickness is relatively small. Another useful feature results from the fact that the pulsed light enhances the contrast without necessarily involving externally staining, as long as there is refractive index difference. The wavelength on-resonance tuning may be used to further enhance the magnitude of the PINEM field, particularly for 'light particles' as in the case of GFP. The PINEM signal is roughly proportional to the fourth power of the particle size, $P_+ \propto a^4$, and consideration of the particle size and photon fluence will determine the overall sensitivity. Finally,

the light polarization may be exploited to obtain tomographic images for different positions and interfaces.

5. Conclusion

In this contribution, we presented a novel approach for electron microscopy imaging using the near field characteristic of nanostructures. By introducing a gating optical pulse to the pump-probe configuration of UEM the temporal resolution of the electron packet can reach the commercially available 10 fs resolution of optical pulses, and possibly the attosecond domain. When using nanoparticles, it is shown that their localized, nanoscale near field enhances imaging contrast which enables the visualization of material interfaces and provides dark field positioning of single particle in cellular system. These temporal and spatial localization features are made *in situ* with the zero of time being well defined

for dynamical studies and maintaining robust the various domains of ultrafast electron microscopy. Our slicing scheme can be utilized not only for gating, but also to directly measure the electron pulse duration with optical precision and *in situ* at the probing region, generally a non-trivial task. We shall explore this capability in a forthcoming publication [37].

Acknowledgements

This work was supported by the National Science Foundation and the Air Force Office of Scientific Research in the Center for Physical Biology funded by the Gordon and Betty Moore Foundation.

References

- [1] A.H. Zewail, J.M. Thomas, 4D Electron Microscopy: Imaging in Space and Time, Imperial College Press, London, 2010.
- [2] A.H. Zewail, Science 328 (2010) 187.
- [3] J.C. Williamson, A.H. Zewail, Chem. Phys. Lett. 209 (1993) 10.
- [4] G. Farkas, C. Toth, Phys. Lett. A 168 (1992) 447.
- [5] F. Krausz, M. Ivanov, Rev. Mod. Phys. 81 (2009) 163.
- [6] P.B. Corkum, F. Krausz, Nat. Phys. 3 (2007) 381.
- [7] T. Brabec, F. Krausz, Rev. Mod. Phys. 72 (2000) 545.
- [8] P. Baum, A.H. Zewail, Proc. Natl. Acad. Sci. U.S.A. 103 (2006) 16105.
- [9] A. Janzen et al., Rev. Sci. Instrum. 78 (2007).
- [10] A. Gahlmann, S.T. Park, A.H. Zewail, Phys. Chem. Chem. Phys. 10 (2008) 2894.
- [11] M. Aidelsburger, F.O. Kirchner, F. Krausz, P. Baum, Proc. Natl. Acad. Sci. U.S.A. 107 (2010) 19714.
- [12] S.A. Hilbert, C. Uiterwaal, B. Barwick, H. Batelaan, A.H. Zewail, Proc. Natl. Acad. Sci. U.S.A. 106 (2009) 10558.
- [13] S. Varro, G. Farkas, Laser Part. Beams 26 (2008) 9.
- [14] P. Baum, A.H. Zewail, Proc. Natl. Acad. Sci. U.S.A. 104 (2007) 18409.
- [15] T. van Oudheusden, E.F. de Jong, S.B. van der Geer, W. Root, O.J. Luiten, B.J. Siwick, J. Appl. Phys. 102 (2007).
- [16] P. Lan, P.X. Lu, W. Cao, Y.H. Li, X.L. Wang, Phys. Rev. A 76 (2007).
- [17] A.F. Lifschitz, J. Faure, Y. Glinec, V. Malka, P. Mora, Laser Part. Beams 24 (2006) 255.
- [18] E. Fill, L. Veisz, A. Apolonski, F. Krausz, New J. Phys. 8 (2006) 272.
- [19] Q. Kong et al., Phys. Rev. E 69 (2004).
- [20] Q. Kong et al., Phys. Plasmas 10 (2003) 4605.
- [21] B. Barwick, D.J. Flannigan, A.H. Zewail, Nature 462 (2009) 902.
- [22] D.J. Flannigan, B. Barwick, A.H. Zewail, Proc. Natl. Acad. Sci. U.S.A. 107 (2010) 9933.
- [23] S.T. Park, M.M. Lin, A.H. Zewail, New J. Phys. 12 (2010) 123028.
- [24] W.D. Kimura et al., Phys. Rev. Lett. 74 (1995) 546.
- [25] K. Mizuno, J. Pae, T. Nozokido, K. Furuya, Nature 328 (1987) 45.
- [26] P.L. Kapitza, P.A.M. Dirac, Proc. Cambridge Philos. Soc. 29 (1933) 297.
- [27] N.M. Kroll, K.M. Watson, Phys. Rev. A 8 (1973) 804.
- [28] A. Weingartshofer, J.K. Holmes, G. Caudle, E.M. Clarke, H. Kruger, Phys. Rev. Lett. 39 (1977) 269.
- [29] M. Abramowitz, I.A. Stegun (Eds.), Handbook of Mathematical Functions, with Formulas, Graphs, and Mathematical Tables, Dover Publications, New York, 1965.
- [30] R.W. Schoenlein et al., Science 287 (2000) 2237.
- [31] M. Chergui, Acta Crystallogr. Sect. A 66 (2010) 229.
- [32] P. Baum, A. Zewail, Chem. Phys. Lett. 462 (2008) 14.
- [33] G. Mie, Ann. Phys.-Berlin 25 (1908) 377.
- [34] J.D. Jackson, Classical Electrodynamics, Wiley, New York, 1975.
- [35] P.B. Johnson, R.W. Christy, Phys. Rev. B 6 (1972) 4370.
- [36] S.A. Maier, Plasmonics: Fundamentals and Applications, Springer, New York, 2007.
- [37] S.T. Park, O.H. Kwon, A.H. Zewail, (in preparation).



Sang Tae Park received Ph.D. in Chemistry from Seoul National University, Korea in 2002. He worked as Research Fellow at the Research Institute of Basic Science of Seoul National University, and then as a Post-doctoral Researcher at California Institute of Technology, Pasadena, USA. Currently, he is Research Scientist at Caltech, where he is studying structural dynamics using ultrafast electron microscopy and diffraction.



Ahmed H. Zewail is the Linus Pauling professor of chemistry and professor of physics, California Institute of Technology (Caltech), USA. He is also the Director of the Physical Biology Center for Ultrafast Science and Technology at Caltech.